Bulletin of the Seismological Society of America, Vol. 104, No. 1, pp. 204–213, February 2014, doi: 10.1785/0120130050

Monitoring a Building Using Deconvolution Interferometry. II: Ambient-Vibration Analysis

by Nori Nakata and Roel Snieder

Abstract Application of deconvolution interferometry to earthquake data recorded inside a building is a powerful technique for monitoring parameters of the building, such as velocities of traveling waves, frequencies of normal modes, and intrinsic attenuation. In this study, we apply interferometry to ambient-vibration data, instead of using earthquake data, to monitor a building. The time continuity of ambient vibrations is useful for temporal monitoring. We show that, because multiple sources simultaneously excite vibrations inside the building, the deconvolved waveforms obtained from ambient vibrations are nonzero for both positive and negative times, unlike the purely causal waveforms obtained from earthquake data. We develop a string model to qualitatively interpret the deconvolved waveforms. Using the synthetic waveforms, we find the traveling waves obtained from ambient vibrations propagate with the correct velocity of the building, and the amplitude decay of the deconvolved waveforms depends on both intrinsic attenuation and ground coupling. The velocities estimated from ambient vibrations are more stable than those computed from earthquake data. Because the acceleration of the observed earthquake records varies depending on the strength of the earthquakes and the distance from the hypocenter, the velocities estimated from earthquake data vary because of the nonlinear response of the building. From ambient vibrations, we extract the wave velocity due to the linear response of the building.

Introduction

Spectral analysis using forced vibrations and/or earthquakes is a common technique to estimate frequencies of normal modes, mode shapes, and viscous damping parameters of a building (Kanai and Yoshizawa, 1961; Trifunac, 1972; Trifunac *et al.*, 2001a,b; Clinton *et al.*, 2006). These parameters are useful for risk assessment and for estimating the response of a building to earthquakes (Michel *et al.*, 2008). The sources listed above are sometimes inappropriate to use for temporal monitoring a building because of the lack of data continuity. Ambient vibrations, caused by sources within the building, are more suitable for monitoring a building because of the quasicontinuous nature of these vibrations (Trifunac, 1972; Ivanović *et al.*, 2000). In this study we use seismic interferometry to analyze ambient vibrations recorded inside a building in the Fukushima prefecture in Japan.

Using seismic interferometry, we can reconstruct waves that propagate from one receiver to another. Seismic interferometry was invented by Aki (1957) and Claerbout (1968) and has been well developed over the last decade (e.g., Lobkis and Weaver, 2001; Derode *et al.*, 2003; Snieder, 2004b; Wapenaar, 2004; Schuster, 2009; Snieder *et al.*, 2009; Tsai, 2011). One can apply seismic interferometry to active sources (e.g., Bakulin and Calvert, 2006; Wegler *et al.*, 2006; Mehta *et al.*, 2008; van der Neut *et al.*, 2011) or to earthquake data (e.g., Sawazaki *et al.*, 2009; Yamada *et al.*, 2010; Nakata and Snieder, 2011, 2012a, b). One can also apply interferometry to noise caused by production (e.g., Miyazawa *et al.*, 2008), drilling (e.g., Vasconcelos and Snieder, 2008a,b), and traffic (e.g., Nakata *et al.*, 2011) and to nonspecific vibrations (so-called "ambient vibration" or "ambient noise") (e.g., Sens-Schönfelder and Wegler, 2006; Brenguier, Campillo, *et al.*, 2008; Brenguier, Shapiro, *et al.*, 2008; Draganov *et al.*, 2009).

In a companion paper (Nakata *et al.*, 2013, henceforth called Part I), we analyze earthquake data, recorded over the same time period in the same building as in this study, using seismic interferometry. Although several studies apply interferometric approaches to earthquake data recorded in a building (e.g., Snieder and Şafak, 2006; Snieder *et al.*, 2006; Kohler *et al.*, 2007; Todorovska and Trifunac, 2008a,b), few studies apply this technique to ambient vibrations (Prieto *et al.*, 2010). As we explain below, by applying seismic interferometry to ambient vibrations recorded in a building, we not only achieve continuous monitoring in time but also obtain information of the ground coupling and linear response of the building, which we cannot estimate from earthquake data.

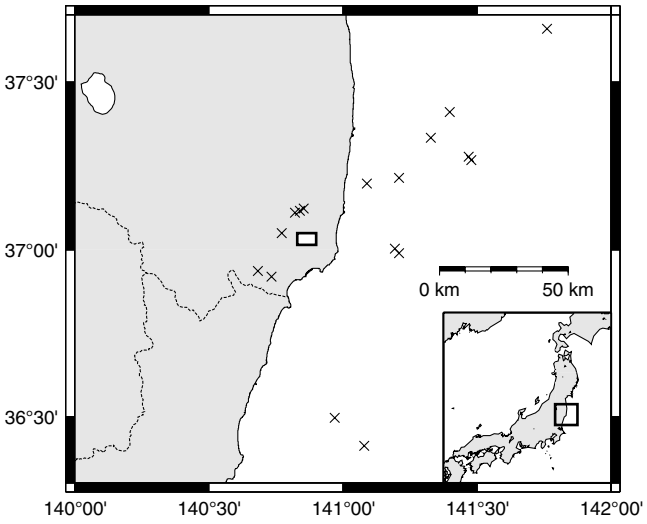

Figure 1. The building (rectangle, not to scale) and epicenters of earthquakes used in Part I (crosses). The inset map indicates the location of the magnified area.

We first introduce ambient-vibration data and deconvolved waveforms computed from the observed data. Next, we analytically and qualitatively interpret the deconvolved waveforms using traveling-wave and normal-mode analyses. Then we monitor the building using ambient vibrations based on the interpretation.

Deconvolution Analysis Using Ambient Vibration

We present data acquisition, preprocessing for deconvolution interferometry, and the interferometry using ambient-vibration data in this section. Data are observed in the same building over the same time period as for the earthquake data in Part I (Fig. 1). Preprocessing has an important role for obtaining reliable correlograms (Bensen *et al.*, 2007), and here we focus on the preprocessing to exclude large amplitudes caused by earthquakes and human activities.

Observed Records

The building we used is in the Fukushima prefecture, Japan (the rectangle in Fig. 1). Continuous ambient seismic vibrations were recorded by Suncoh Consultants Co., Ltd. for two weeks (31 May–14 June 2011) using 10 MEMS accelerometers developed by Akebono Brake Industry Co., Ltd. The building has eight stories, a basement, and a penthouse (Fig. 2). Based on the analysis in Part I, the waves, which propagate vertically inside the building, reflect off the top of the penthouse (R2 in Fig. 2). The sampling interval of the accelerometers is 1 ms, and the receivers have vertical, east–west horizontal, and north–south horizontal components. In this study we focus on the east–west horizontal component to extract horizontal modes.

Figure 3 illustrates the root mean square (rms) amplitude computed over a moving window with a duration of 30 s of unfiltered seismic records observed for the two weeks. The

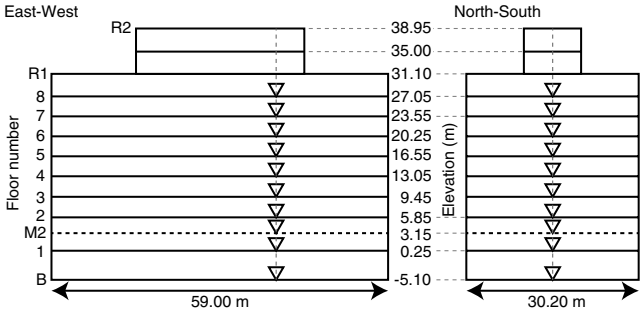

Figure 2. The (left) east–west and (right) north–south vertical cross sections of the building and the positions of receivers (triangles). Elevations denote the height of each floor from ground level. Receivers are located on stairs 0.19 m below each floor, except for the basement (on the floor) and the first floor (0.38 m below). Receiver M2 is located between the first and second floors. Horizontal components of receivers are aligned with the east–west and north–south directions.

hours of operation of the building are from 8 a.m. to 6 p.m. on weekdays, when the rms amplitude is elevated. On the weekends we observe lower rms amplitudes (4 June, 5 June, 11 June, and 12 June are weekends, shown as shaded areas in Fig. 3). The vibrations are probably induced by human activities, elevators, air conditioners, computers, traffic near the building, and other sources. Amplitudes at the upper floors are stronger due to the shape of the fundamental mode of the building (see fig. 4 in Part I for the shape of the fundamental mode). Stronger amplitudes at the first floor compared with nearby floors may be caused by vibrations from traffic outside the building and/or many visitors to that floor. Because the amplitudes at the basement are much smaller than the other floors, we do not interpret the records at the basement in this study.

Preprocessing

Before applying deconvolution interferometry, we exclude large-amplitude intervals from the continuous records because we focus on ambient vibrations. Large amplitudes are excited by earthquakes and human interference, such as people touching the accelerometers. Because receivers are often located at places where people can touch them (e.g., on stairs), a technique proposed here to exclude the human interference is useful. To exclude large-amplitude waves, we apply a data-weighting procedure based on the standard deviation of data recorded for one hour in which the data do not include significant earthquakes or human interference (Wegler and Sens-Schönfelder, 2007). When one receiver records a larger amplitude than the threshold, the samples of all receivers at that time are set to zero because we need the waveforms at the same time at all sensors for the deconvolution analysis. After someone touches a receiver, the DC component on the seismograms may change. We subtract the DC component from the data of every 30 s and discard data when the DC component changes during each time interval.

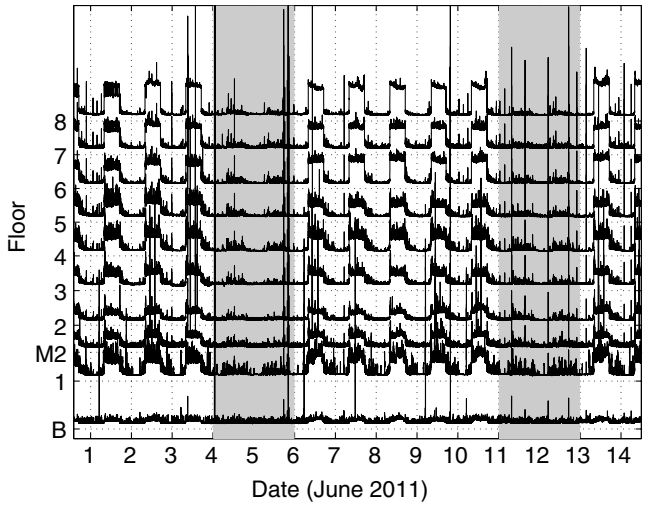

Figure 3. The rms amplitude of the records observed at each floor. The labels of the date are placed at the start of days (midnight). Each trace indicates the rms amplitude, and the positive axis of amplitude for each trace is upward (dashed horizontal grids describe zero amplitude at each floor). The shaded areas correspond to weekends.

Similar to large amplitudes, we exclude time intervals when one receiver indicates a change in the DC component.

Deconvolution Analysis Using Two-Week Ambient Vibration

We apply deconvolution interferometry to ambient-vibration records observed inside the building. Here, we stack deconvolved waveforms over the two weeks in which data were collected. In the Monitoring the Building Using Ambient Vibration section, we stack over four-day intervals for monitoring purposes. We deconvolve each 30 s ambient-vibration record with the first-floor record and then stack the waveforms over the two week interval:

$$D(z,t) = \sum_{n=1}^{N}\left[\mathcal{F}^{-1}\left\{\frac{u_n(z,\omega)}{u_n(0,\omega)}\right\}\right]$$
$$\approx \sum_{n=1}^{N}\left[\mathcal{F}^{-1}\left\{\frac{u_n(z,\omega)u_n^*(0,\omega)}{|u_n(0,\omega)|^2+\alpha\langle|u_n(0,\omega)|^2\rangle}\right\}\right], \qquad (1)$$

in which N is the number of 30 s intervals (40,080 in this study), $u_n(z,\omega)$ is the nth wavefield in the frequency domain recorded at z ($z=0$ is the first floor), ω is the angular frequency, t is time, $\mathcal{F}^{-1}$ is the inverse Fourier transform, $*$ is the complex conjugate, $\langle|u_n|^2\rangle$ is the average power spectrum of u_n, and $\alpha = 0.5\%$ is a regularization parameter stabilizing the deconvolution (Clayton and Wiggins, 1976). Our Fourier convention is $f(t) = \int_{-\infty}^{\infty} F(\omega)e^{-i\omega t}d\omega$. We apply a band-pass filter, 1.5–15 Hz, to the deconvolved waveforms (Fig. 4).

In Figure 4, we obtain traveling waves and the fundamental mode for both positive and negative times, unlike the deconvolved waveforms obtained from earthquake data, which only contain the causal waves (Part I). Because deconvolution interferometry creates a virtual source exciting waves at $t = 0$ (Snieder *et al.*, 2006), causal and acausal waves refer to the waves in the positive and negative times, respectively. The waveforms in Figure 4 are almost symmetric in time. We estimate the velocity from the downgoing wave in the positive time and the upgoing wave in the negative time (marked by the arrows in Fig. 4) using the least-squares fitting of picked arrival times (see Part I for the detail of the method). The velocity thus obtained is 270 ± 5 m/s, in which the uncertainty is one standard deviation of the estimated velocities at each floor (the gray lines in Fig. 4). We do not use the upgoing wave in the positive time and the downgoing wave in the negative time because these waves overlap and we cannot accurately pick their arrival times.

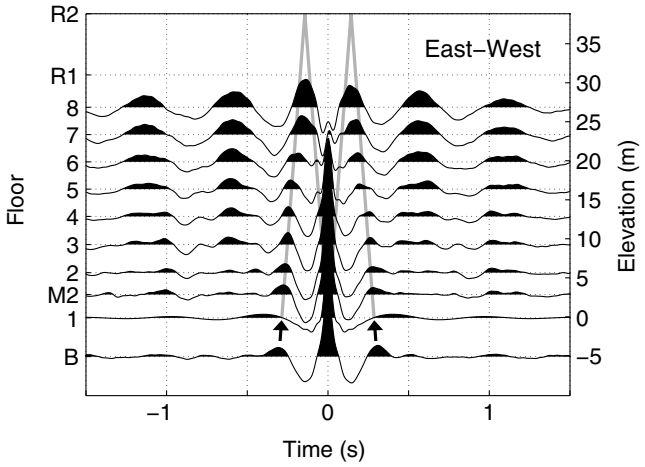

Figure 4. Deconvolved waveforms obtained from ambient vibrations in the east–west component (expression 1). Ambient vibrations observed at floor 1 is used for the denominator in expression (1). The waveforms are averaged over two weeks and applied a band-pass filter 1.5–15 Hz. The traveling-wave velocity is estimated from the downgoing waves in the positive time and the upgoing waves in the negative time (marked by arrows). Gray lines show the arrival times of the waves propagating with a velocity equal to 270 m/s.

If we estimate a quality factor ($Q^{(ar)}$) from the amplitude decay of the waveforms in Figure 4 using the technique in Part I, in which we time-reverse the waveforms to estimate $Q^{(ar)}$ for the acausal part, the obtained values of $Q^{(ar)}$ are 25.3 and 20.2 in the causal and acausal parts, respectively. We explain below that the amplitude decay does not only depend on the intrinsic attenuation in the building when we use ambient vibrations; the decay of the waveforms reconstructed from ambient vibrations is also affected by radiation losses due to the ground coupling. The superscripts of $Q^{(ar)}$ indicate that the quality factor is effected by intrinsic attenuation (a) and radiation damping (r). Note that the quality factor estimated from earthquake data indicates only intrinsic attenuation ($Q^{(a)}$). In Part I, we obtain $Q^{(a)} = 10.2$ for the largest earthquake, which gives the lowest value of $Q^{(a)}$; the estimated $Q^{(a)}$ from each earthquake varies between 10 and 40 because of the difference of the strength of shaking. As explained below, further research is needed to estimate the

relationship between $Q^{(ar)}$ and $Q^{(a)}$. Hereafter, we use Q without a superscript to refer to the intrinsic attenuation ($Q^{(a)}$).

Discussion of the Deconvolved Waveforms

In this section, we interpret the deconvolved waveforms in Figure 4 using a mathematical description and synthetic waveforms based on traveling waves and normal modes. The goals of this section are to understand why we obtain both causal and acausal waves after applying interferometry to ambient vibrations, to reconstruct the waveforms using synthetic computation, and to determine to what degree we can estimate the velocity of traveling waves and the quality factor from ambient vibrations. The main differences of deconvolved waveforms obtained from ambient vibrations and earthquakes are that for ambient vibrations, sources are inside the building and more than one source simultaneously excites inside and outside the building. We consider deconvolved waveforms computed from one source inside the building based on traveling waves and from multiple sources based on normal modes.

One Source inside the Building

To analyze deconvolved waveforms obtained from one source inside the building, we employ the same assumptions as equation (1) in Part I: vertically propagating waves in the building, constant amplitude and wavenumber, no torsional waves, and no internal reflections. Based on Snieder and Şafak (2006) and Part I, when a source is at height z_s, the observed record at an arbitrary receiver at height z is

$$u(z > z_s, \omega) = S(\omega) \frac{X}{1 - Re^{2ikH} e^{-2\gamma|k|H}} \tag{2}$$

for $z > z_s$, and

$$u(z < z_s, \omega) = S(\omega) \frac{X'}{1 - Re^{2ikH} e^{-2\gamma|k|H}} \tag{3}$$

for $z < z_s$. Here, $S(\omega)$ is the source function, R is the reflection coefficient at the base of the building, k is the wavenumber, γ is the attenuation coefficient, H is the height of the building, and i is the imaginary unit. The attenuation coefficient is defined by $\gamma = 1/(2Q)$ (Aki and Richards, 2002). The numerators X and X' are given by

$$X = e^{ik(z-z_s)} e^{-\gamma|k|(z-z_s)} + e^{ik(2H-z-z_s)} e^{-\gamma|k|(2H-z-z_s)} + R[e^{ik(z+z_s)} e^{-\gamma|k|(z+z_s)} + e^{ik(2H-z+z_s)} e^{-\gamma|k|(2H-z+z_s)}],$$

and

$$X' = e^{ik(z_s-z)} e^{-\gamma|k|(z_s-z)} + e^{ik(2H-z-z_s)} e^{-\gamma|k|(2H-z-z_s)} + R[e^{ik(z+z_s)} e^{-\gamma|k|(z+z_s)} + e^{ik(2H-z_s+z)} e^{-\gamma|k|(2H-z_s+z)}],$$

respectively.

The waveforms recorded at height z deconvolved with the waveform recorded at the first floor ($z = 0$) are

$$D(z>z_s,\omega) = \frac{u(z>z_s)}{u(z=0)} = \frac{[e^{ik(z-2z_s)} e^{-\gamma|k|(z-2z_s)} + Re^{ikz} e^{-\gamma|k|z}][1+e^{2ik(H-z)} e^{-2\gamma|k|(H-z)}]}{1+R} \times \sum_{n=0}^{\infty} (-1)^n [e^{2ink(H-z_s)} e^{-2n\gamma|k|(H-z_s)}], \tag{4}$$

and

$$D(z<z_s,\omega) = \frac{u(z<z_s)}{u(z=0)} = \frac{e^{-ikz} e^{\gamma|k|z} + Re^{ikz} e^{-\gamma|k|z}}{1+R}. \tag{5}$$

From expressions (4) and (5), the deconvolved waveforms obtained from one source inside the building are dependent on the ground coupling; this is in contrast to the case in which sources are outside the building (i.e., earthquakes). Interestingly, although the deconvolved waveforms retrieved from external sources are only related to the structure of the building (Part I), the waveforms from internal sources are governed by both the structure of the building and the ground coupling (through the reflection coefficient R).

We numerically compute synthetic observed records based on expressions (2) and (3) (Fig. 5a) and deconvolve these records with the waveform recorded at $z = 0$ m (Fig. 5b). The model parameters to compute the waveforms in Figure 5a are $H = 39$ m, $R = -0.6$, $Q = 30$, and $c = 270$ m/s, in which c is the velocity of the traveling wave in the building. The waves are excited at $z_s = 13$ m at $t = 0.2$ s. The gray lines in Figure 5b indicate the arrival times of traveling waves estimated from expression (4) for above the source ($z > z_s$) and expression (5) for below the source ($z < z_s$). After deconvolution we obtain acausal waves in Figure 5b. These waves correspond to the term $e^{ik(z-2z_s)} e^{-\gamma|k|(z-2z_s)}$ in expression (4) and $e^{-ikz} e^{\gamma|k|z}$ in expression (5). Note that these acausal waves exist only for a time interval $-z_s/c < t < 0$ (-0.05 s $< t < 0$ s in Fig. 5b) and that the waves are not symmetric in time. Therefore, one source in the building does not explain the symmetry between the acausal and causal waves in Figure 4.

Multiple Sources

Using the normal-mode theory (Snieder, 2004a, chapter 20), we compute the deconvolved waveforms obtained from multiple sources to qualitatively interpret the waveforms in Figure 4. We can express waves using either the summation of traveling waves or normal modes (Dahlen and Tromp, 1998, chapter 4; Snieder and Şafak, 2006). Equations (2)–(5) are based on traveling waves, and these equations depend on the location of sources. We have to modify all terms in the numerators of equations (2) and (3) and choose equations (2) or (3) depending on the locations of receiver and source. On the other hand, the normal-mode analysis is suitable for multiple sources inside the building because source terms are

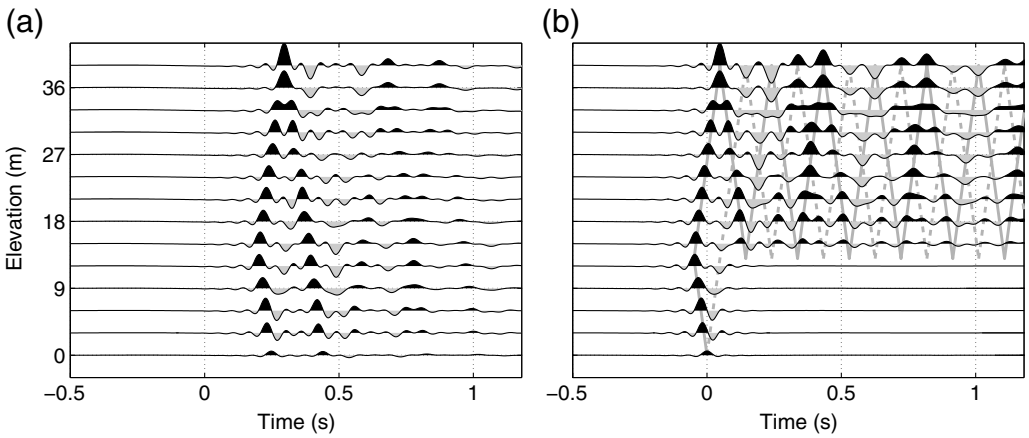

Figure 5. (a) Synthetic waveforms obtained from one source inside a building (expressions 2 and 3) and (b) waveforms of panel (a) after deconvolution with the waves observed at $z = 0$ m. The source is located at $z_s = 13$ m and excites waves at $t = 0.2$ s. The gray lines in panel (b) show the arrival times of the traveling waves based on expressions (4) and (5). The solid and dashed gray lines illustrate the terms $e^{ik(z-2z_s)}e^{-\gamma|k|(z-2z_s)}$ and $Re^{ikz}e^{-\gamma|k|z}$, respectively, and their reverberations. The amplitudes of panels (a) and (b) are normalized after applying the same band-pass filter as used in Figure 4.

separated from other terms (e.g., equation 20.69 in Snieder, 2004a).

The model for our normal-mode analysis is a 1D string model that includes radiation damping (Snieder, 2004a, chapter 20.10). This model consists of an open-ended light string with mass density ρ connected to a heavy string with density $\rho_g \gg \rho$ at $z = 0$ (Fig. 6). The wave propagation in the light and heavy strings represents the propagation in the building and the subsurface, respectively. Although the string model is primitive, the model qualitatively accounts for the wave propagation in the building because of three reasons; (1) we are only interested in the building, (2) the effect of the ground for the building is limited to the coupling at $z = 0$, and (3) we assume no waves return after the waves propagate to the ground. The ratio of the densities of the light and heavy strings is related to the reflection coefficient at the connection of the strings (at the base of the building) (Coulson and Jeffrey, 1977, chapter 2):

$$R = \frac{\sqrt{\rho} - \sqrt{\rho_g}}{\sqrt{\rho} + \sqrt{\rho_g}} = \frac{-1 + \epsilon}{1 + \epsilon}, \tag{6}$$

in which

$$\epsilon = \sqrt{\rho/\rho_g}. \tag{7}$$

We carry out a perturbation analysis for this small dimensionless parameter.

The eigenfunctions and eigenfrequencies of this string model to first order in ϵ for the mode m $(m = 0, 1, \cdots)$ are given by

$$u_m(z) = \sin\left[\pm\left(m + \frac{1}{2}\right)\frac{\pi z}{H}\right] - i\epsilon\frac{H - z}{H}\cos\left[\pm\left(m + \frac{1}{2}\right)\frac{\pi z}{H}\right], \tag{8}$$

and

$$\omega_m^{(r)} = \left[\pm\left(m + \frac{1}{2}\right)\pi - i\epsilon\right]\frac{c}{H}, \tag{9}$$

respectively (see Appendix). Because this string model does not include the intrinsic attenuation of the building, the eigenfrequency in expression (9) does not incorporate the attenuation. The superscript in expression (9) indicates that the complex eigenfrequency accounts only for the radiation loss. Snieder and Şafak (2006) derive the eigenfrequency $(\omega_m^{(a)})$ with the intrinsic attenuation, but without radiation damping:

$$\omega_m^{(a)} = \left(m + \frac{1}{2}\right)\frac{\pi c}{H}(\pm 1 - i\gamma). \tag{10}$$

Comparing expressions (9) and (10), we account for the intrinsic attenuation and the radiation damping using the eigenfrequency

$$\omega_m^{(ar)} = \left[\pi\left(m + \frac{1}{2}\right)(\pm 1 - i\gamma) - i\epsilon\right]\frac{c}{H}, \tag{11}$$

for which we assume the intrinsic attenuation to be weak and ignore a cross term between the intrinsic attenuation and radiation damping. In expression (11), the first term, $\pi(m + 1/2)c/H$, is the frequency in case there is no intrinsic attenuation ($\gamma = 0$) and the building has a rigid boundary at the bottom ($R = -1$). The second term, $-i\gamma\pi(m + 1/2)c/H$, accounts for the intrinsic attenuation, and the third term, $-i\epsilon c/H$, accounts for the radiation loss at the base of the building. The waveforms in this string model with the intrinsic attenuation are given by the summation of normal modes (Snieder, 2004a):

$$u(z, \omega) = \sum_{m=0}^{\infty} \frac{u_m(z)\int u_m^*(z')F(z')dz'}{(\omega_m^{(ar)})^2 - \omega^2}, \tag{12}$$

in which F indicates the forces that excite the vibrations.

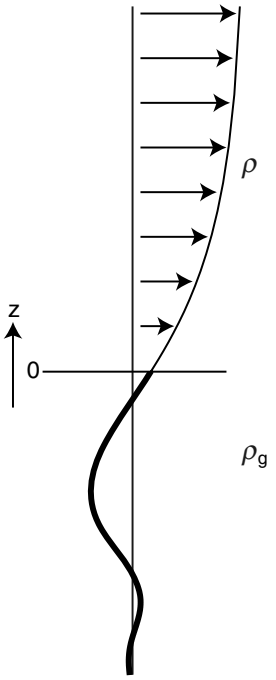

Figure 6. Displacement of radiation damping of the string model. The density of the light string (ρ; $z > 0$; thin line) is much smaller than that of the heavy string (ρ_g; $z < 0$; thick line).

We numerically compute the synthetic records using expression (12) for various values of the quality factor Q and the reflection coefficient R with fixed parameters: $H = 39$ m and $c = 270$ m/s. We use random sources (random amplitude, phase, origin time, and location) and compute three-hour random-source synthetic observed records. Then we deconvolve the waveforms with the records at the floor at $z = 0$ (Fig. 7). All panels in Figure 7 show waves for both positive and negative times, which is consistent with the deconvolved waveforms in Figure 4. Especially for $|t| \gtrsim 1$ s, the waveforms in Figure 7 are similar in character to those in Figure 4. For $|t| \lesssim 0.3$ s, we obtain the traveling waves, propagating with the same velocity as used for the modeling ($c = 270$ m/s; compare the waveforms and the gray lines in Fig. 7).

The waveforms are increasingly asymmetric in time as the reflection coefficient differs from $R = -1$, or as the anelastic damping increases (e.g., Fig. 7d–f or 7b,e,h). From Figure 7, we learn that the amplitude decay of the waveforms is related to the intrinsic attenuation and the boundary condition. Based on the similarity of the waveforms in Figures 4 and 7, the reflection coefficient and the quality factor of the real building are likely close to those in Figure 7a–e. Because we can estimate $Q^{(a)}$ independent from the ground coupling using the earthquake data (Part I), the deconvolution using ambient vibrations is potentially useful for estimating R. However, to estimate R, we need a more quantitative analysis, which is a topic of future work. Also, for waveform matching this string model may be too simple. We conclude that the estimated velocity from the waveforms in Figure 4 indicates the true velocity of the traveling wave in the building, and the quality factor estimated from the amplitude decay of the waveforms is $Q^{(ar)}$ not just $Q^{(a)}$. In the next section, we monitor the velocity of the building.

Monitoring the Building Using Ambient Vibration

For monitoring the velocity of the traveling waves, we need to know the minimum time length to obtain stable deconvolved waveforms. To determine this time interval, we compute the convergence of the deconvolved waveforms as a function of the stacking duration h using an rms misfit as used by Prieto *et al.* (2010):

$$\text{Misfit}(z,h) = \sqrt{\frac{\int_{t_a}^{t_b}[D_h(z,t) - D_{\text{all}}(z,t)]^2 dt}{\int_{t_a}^{t_b}[D_{\text{all}}(z,t)]^2 dt}}, \qquad (13)$$

in which t_a and t_b define the time interval to compute the misfit (-1.5 s and 1.5 s in this study), h is the stacking duration, D_h is the deconvolved waves stacked over time period h, and D_{all} is the deconvolved waveforms obtained from the entire data set recorded during the two weeks. If the rms misfit is small, the deconvolved waveform D_h is similar to the deconvolved waveforms obtained from the entire data set.

Figure 8 indicates the convergence of deconvolved waveforms with respect to the stacking duration. In Figure 8a, we use both daytime (8 a.m.–6 p.m.) and nighttime (6 p.m.–8 a.m.) data. Because the rms misfit is lower than 5% when we use the ambient-vibration data longer than 96 hours, we decide that stacking over 96 hours is sufficient to obtain stable deconvolved waveforms. The rms misfit in Figure 8a increases during some nighttimes. However, because the rms misfits at $h = 66$ are smaller than the misfits at $h = 52$ at all floors, for example, the vibrations in nighttime also contribute to the convergence. We also compute the waveforms using daytime data only and estimate the rms misfit (Fig. 8b). Interestingly, although Figure 8b shows rapid convergence to 10%, we need about 40 hours (equivalent to four days) to obtain the rms misfit lower than 5%. In Figure 8, we show the rms misfits for 122 hours (panel a) and for 52 hours (panel b), which are equivalent because 122 hours include 52 hours of daytime and 70 hours of nighttime.

Figure 9 shows the deconvolved waveforms using the data recorded during both daytime and nighttime (same data as used in Fig. 8a), and Figure 10 using the data recorded during daytime only (same data as used in Fig. 8b). In Figure 9, we stack the data over four-day intervals (96 hours) and overlap these intervals over two days. From the waveforms in Figure 9, we estimate the velocity of the traveling waves using the same method as Figure 4. The estimated velocities are stable during the two weeks, and the uncertainty is about 6 m/s, which is smaller than the uncertainty in the velocity estimated from earthquake data (fig. 12 in Part I). Figure 11 shows a comparison of velocities estimated from ambient vibrations and earthquakes. For earthquakes, the estimated velocities vary more than for ambient vibrations,

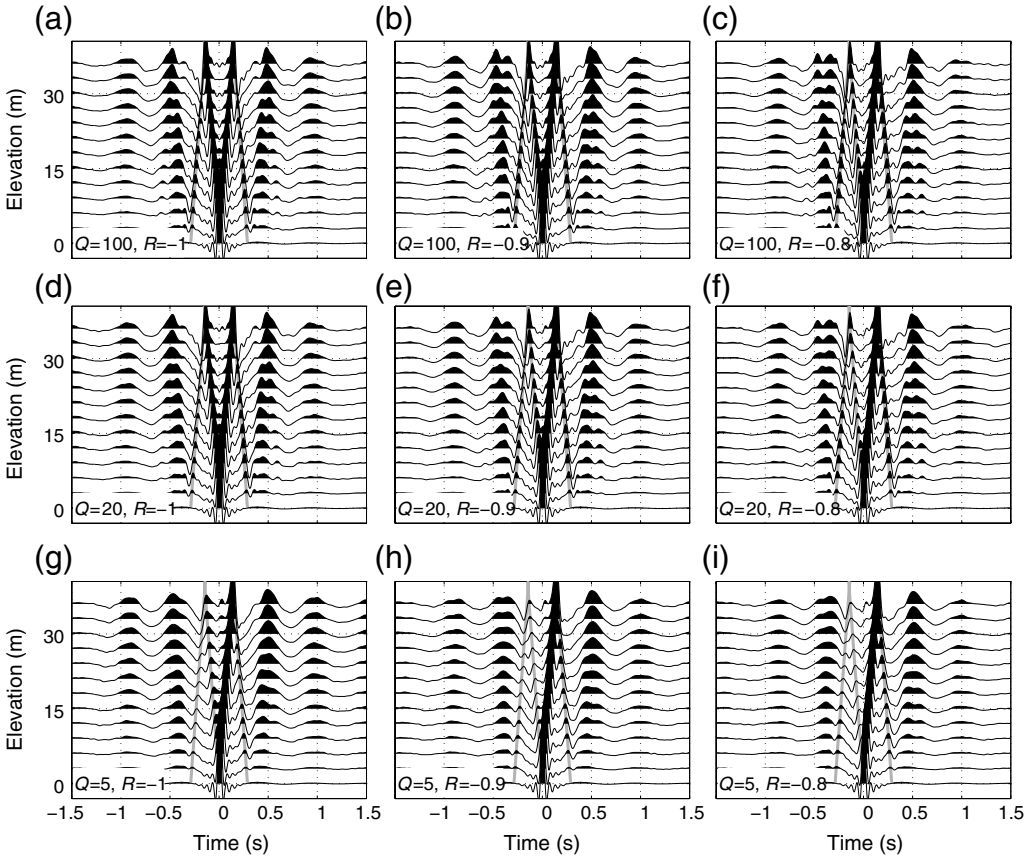

Figure 7. Synthetic deconvolved waveforms using three hour random vibrations as sources after applying the same band-pass filter as in Figure 4. Panels (a)–(i) are computed by adopting different quality factors Q and reflection coefficients R (see lower left of each panel). Gray lines indicate the arrival time of the traveling wave with the velocity used for the modeling ($c = 270$ m/s). The scale of the amplitudes at each panel is the same.

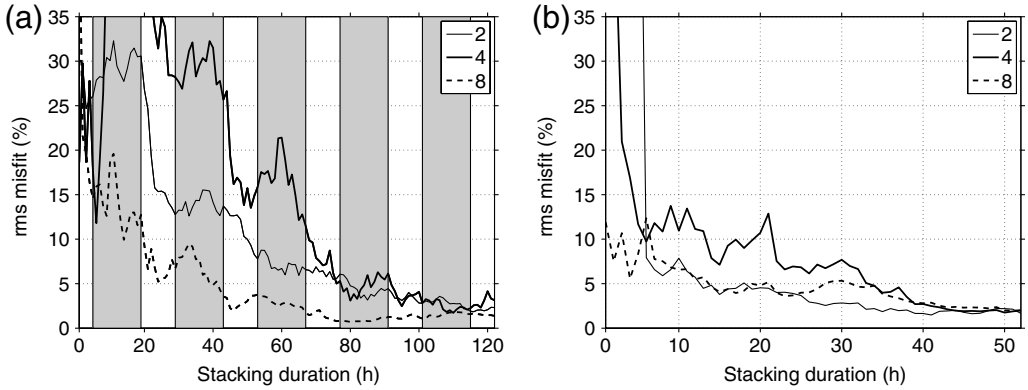

Figure 8. Convergence test of ambient-vibration interferometry based on rms misfits (equation 13) as a function of the stacking duration. (a) The rms misfits with respect to the stacked waveform over two-week ambient vibrations, recorded in both daytime (8 a.m.–6 p.m.) and nighttime (6 p.m.–8 a.m.). The shaded areas correspond to night times. We show the misfits at the second, fourth, and eighth floors. (b) The rms misfits with respect to the same waveforms as panel (a), but using only daytime data. We show the rms misfits for 122 hours (52 hours of daytime and 70 hours of nighttime) in panel (a) and 52 hours in panel (b).

and the acceleration of the observed records also varies (fig. 12b in Part I). These variations indicate that the velocities estimated from earthquakes include nonlinear effects. The velocities estimated from ambient vibrations are not affected by nonlinearity because the acceleration of the observed records is small and does not vary much. Therefore, ambient vibration is appropriate for monitoring the velocity of traveling waves in the linear regime. Deconvolved waveforms in Figure 10 are similar to those in Figure 9, and the differences in estimated velocities are not statistically significant.

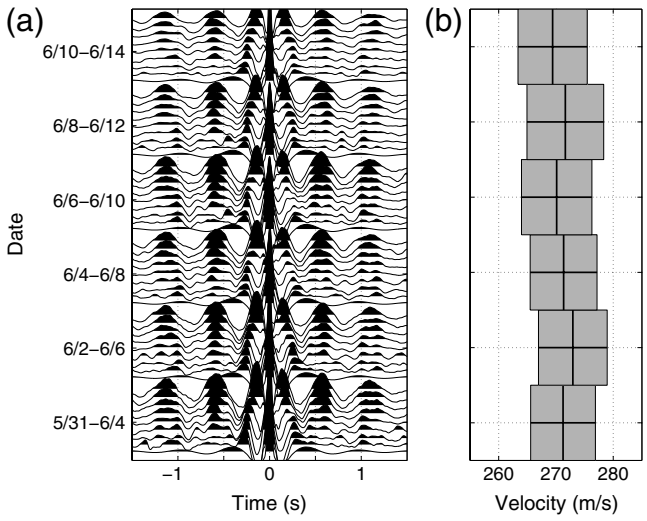

Figure 9. (a) Time-lapse deconvolved waveforms averaged over 96 hours with a 48 hour overlap using ambient vibrations recorded in both daytime and nighttime. We have applied the same band-pass filter as used in Figure 4. (b) Shear-wave velocities estimated from the traveling waves in panel (a). The width of each box indicates one standard deviation of estimated velocities at each floor.

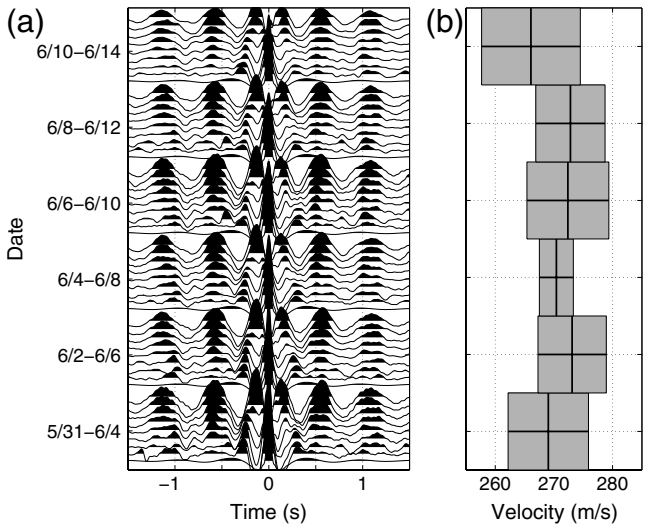

Figure 10. (a) Time-lapse deconvolved waveforms averaged over 40 hours, with a 20 hour overlap using ambient vibration recorded in daytime only. We have applied the same band-pass filter as used in Figure 4. (b) Shear-wave velocities estimated from the traveling waves in panel (a). The width of each box indicates one standard deviation of estimated velocities at each floor.

Conclusions

We retrieve traveling waves inside the building by applying seismic interferometry to ambient-vibration data. In contrast to the case in which sources are only outside the building (i.e., earthquakes), deconvolved waves obtained from ambient vibrations are nonzero for both positive and negative times, which is explained because multiple sources simultaneously excite inside the building. Based on the normal-mode analysis, we synthetically reconstruct waveforms that are qualitatively similar to the real data using the simple string model. The velocity estimated from the synthetic waveforms with this model is the same as the true velocity although the attenuation estimated from the decay of the amplitude with time is not equal to the intrinsic attenuation of the building. Because the amplitude decay is also influenced by radiation losses at the base of the building, we are, in principle, able to estimate both quality factors and reflection coefficients separately from the amplitude of the waveforms, which requires a more accurate model than the string model used here. For monitoring the building, we find the time interval to obtain stable waveforms using the convergence test, and we need deconvolved ambient vibrations averaged over four days to obtain stable waveforms for this building. The velocity estimated from ambient-vibration data is more stable than that from earthquake data because the ambient vibrations are due to the linear response of the building.

Data and Resources

Seismograms used in this study were operated and maintained by Suncoh Consultants Co., Ltd. Figure 1 was produced using Generic Mapping Tools (GMT; available at http://gmt.soest.hawaii.edu, last accessed June 2013).

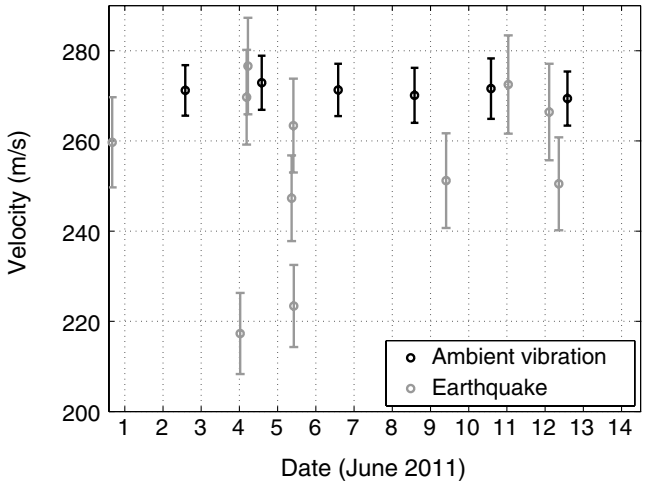

Figure 11. Velocities estimated from ambient vibrations recorded in both daytime and nighttime (black) and earthquakes using a stretching method in Part I (gray). The labels of the date are placed at the start of days (midnight). The velocities in black are plotted at the center of each 96 hour interval and those in the gray are at the origin time of each earthquake. The error bars correspond to the bars shown in figures 9 and 12 in Part I, respectively.

Acknowledgments

We want to thank Suncoh Consultant Co., Ltd. and Akebono Brake Industry Co., Ltd. for providing the data. We thank Seiichiro Kuroda for his professional comments to improve this work. N.N. thanks the instructor and classmates of the class Academic Publishing in Colorado School of Mines for their help in preparing this manuscript. This work was supported

by the Consortium Project on Seismic Inverse Methods for Complex Structures at the Center for Wave Phenomena.

References

Aki, K. (1957). Space and time spectra of stationary stochastic waves, with special reference to microtremors, *Bull. Earthq. Res. Inst.* **35,** 415–456.

Aki, K., and P. G. Richards (2002). *Quantitative Seismology*, 2nd Ed., Univ. Science Books, Sausalito, California, 700 pp.

Bakulin, A., and R. Calvert (2006). The virtual source method: Theory and case study, *Geophysics* **71,** no. 4, S1139–S1150.

Bensen, G. D., M. H. Ritzwoller, M. P. Barmin, A. L. Levshin, F. Lin, M. P. Moschetti, N. M. Shapiro, and Y. Yang (2007). Processing seismic ambient noise data to obtain reliable broad-band surface wave dispersion measurements, *Geophys. J. Int.* **169,** 1239–1260.

Brenguier, F., M. Campillo, C. Hadziioannou, N. M. Shapiro, R. M. Nadeau, and E. Larose (2008). Postseismic relaxation along the San Andreas Fault at Parkfield from continuous seismological observations, *Science* **321,** 1478–1481.

Brenguier, F., N. M. Shapiro, M. Campllo, V. Ferrazzini, Z. Duputel, O. Coutant, and A. Nercessian (2008). Towards forecasting volcanic eruptions using seismic noise, *Nature Geosci.* **1,** 126–130.

Claerbout, J. F. (1968). Synthesis of a layered medium from its acoustic transmission response, *Geophysics* **33,** no. 2, 264–269.

Clayton, R. W., and R. A. Wiggins (1976). Source shape estimation and deconvolution of teleseismic bodywaves, *Geophys. J. Roy. Astron. Soc.* **47,** 151–177.

Clinton, J. F., S. C. Bradford, T. H. Heaton, and J. Favela (2006). The observed wander of the natural frequencies in a structure, *Bull. Seismol. Soc. Am.* **96,** no. 1, 237–257.

Coulson, C. A., and A. Jeffrey (1977). *Waves: A Mathematical Approach to the Common Types of Wave Motion*, 2nd Ed., Longman, United Kingdom, 240 pp.

Dahlen, F. A., and J. Tromp (1998). *Theoretical Global Seismology*, Princeton University Press, Princeton, New Jersey, 944 pp.

Derode, A., E. Larose, M. Tanter, J. de Rosny, A. Tourin, M. Campillo, and M. Fink (2003). Recovering the Green's function from field-field correlations in an open scattering medium (L), *J. Acoust. Soc. Am.* **113,** no. 6, 2973–2976.

Draganov, D., X. Campman, J. Thorbecke, A. Verdel, and K. Wapenaar (2009). Reflection images from ambient seismic noise, *Geophysics* **74,** no. 5, A63–A67.

Ivanović, S. S., M. D. Trifunac, and M. I. Todorovska (2000). Ambient vibration tests of structures—A review, *ISET J. Earthq. Tech.* **37,** no. 4, 165–197.

Kanai, K., and S. Yoshizawa (1961). On the period and the damping of vibration in actual buildings, *Bull. Earthq. Res. Inst.* **39,** 477–489.

Kohler, M. D., T. H. Heaton, and S. C. Bradford (2007). Propagating waves in the steel, moment-frame Factor building recorded during earthquakes, *Bull. Seismol. Soc. Am.* **97,** no. 4, 1334–1345.

Lobkis, O. I., and R. L. Weaver (2001). On the emergence of the Green's function in the correlations of a diffuse field, *J. Acoust. Soc. Am.* **110,** no. 6, 3011–3017.

Mehta, K., J. L. Sheiman, R. Snieder, and R. Calvert (2008). Strengthening the virtual-source method for time-lapse monitoring, *Geophysics* **73,** no. 3, S73–S80.

Michel, C., P. Guéguen, and P.-Y. Bard (2008). Dynamic parameters of structures extracted from ambient vibration measurements: An aid for the seismic vulnerability assessment of existing buildings in moderate seismic hazard regions, *Soil Dynam. Earthq. Eng.* **28,** 593–604.

Miyazawa, M., R. Snieder, and A. Venkataraman (2008). Application of seismic interferometry to extract *P*- and *S*-wave propagation and observation of shear-wave splitting from noise data at Cold Lake, Alberta, Canada, *Geophysics* **73,** no. 4, D35–D40.

Nakata, N., and R. Snieder (2011). Near-surface weakening in Japan after the 2011 Tohoku-Oki earthquake, *Geophys. Res. Lett.* **38,** L17302, doi: 10.1029/2011GL048800.

Nakata, N., and R. Snieder (2012a). Estimating near-surface shear-wave velocities in Japan by applying seismic interferometry to KiK-net data, *J. Geophys. Res.* **117,** no. B01308, doi: 10.1029/2011JB008595.

Nakata, N., and R. Snieder (2012b). Time-lapse change in anisotropy in Japan's near surface after the 2011 Tohoku-Oki earthquake, *Geophys. Res. Lett.* **39,** L11313, doi: 10.1029/2012GL051979.

Nakata, N., R. Snieder, S. Kuroda, S. Ito, T. Aizawa, and T. Kunimi (2013). Monitoring a building using deconvolution interferometry, I: Earthquake-data analysis, *Bull. Seismol. Soc. Am.* **103,** no. 3, 1662–1678, doi: 10.1785/0120120291.

Nakata, N., R. Snieder, T. Tsuji, K. Larner, and T. Matsuoka (2011). Shear-wave imaging from traffic noise using seismic interferometry by cross-coherence, *Geophysics* **76,** no. 6, SA97–SA106, doi: 10.1190/GEO2010-0188.1.

Prieto, G. A., J. F. Lawrence, A. I. Chung, and M. D. Kohler (2010). Impulse response of civil structures from ambient noise analysis, *Bull. Seismol. Soc. Am.* **100,** no. 5A, 2322–2328.

Sawazaki, K., H. Sato, H. Nakahara, and T. Nishimura (2009). Time-lapse changes of seismic velocity in the shallow ground caused by strong ground motion shock of the 2000 western-Tottori earthquake, Japan, as revealed from coda deconvolution analysis, *Bull. Seismol. Soc. Am.* **99,** no. 1, 352–366.

Schuster, G. (2009). *Seismic Interferometry*, Cambridge Univ. Press, New York, 260 pp.

Sens-Schönfelder, C., and U. Wegler (2006). Passive image interferometry and seasonal variations of seismic velocities at Merapi Volcano, Indonesia, *Geophys. Res. Lett.* **33,** L21302, doi: 10.1029/2006GL027797.

Snieder, R. (2004a). *A Guided Tour of Mathematical Methods for the Physical Sciences*, Cambridge Univ. Press, United Kingdom, 507 pp.

Snieder, R. (2004b). Extracting the Green's function from the correlation of coda waves: A derivation based on stationary phase, *Phys. Rev. E* **69,** 046,610.

Snieder, R., and E. Şafak (2006). Extracting the building response using seismic interferometry: Theory and application to the Millikan Library in Pasadena, California, *Bull. Seismol. Soc. Am.* **96,** no. 2, 586–598.

Snieder, R., M. Miyazawa, E. Slob, I. Vasconcelos, and K. Wapenaar (2009). A comparison of strategies for seismic interferometry, *Surv. Geophys.* **30,** no. 10, 503–523.

Snieder, R., J. Sheiman, and R. Calvert (2006). Equivalence of the virtual-source method and wave-field deconvolution in seismic interferometry, *Phys. Rev. E* **73,** 066,620.

Todorovska, M. I., and M. D. Trifunac (2008a). Earthquake damage detection in the Imperial Country Services Building III: Analysis of wave travel times via impulse response functions, *Soil Dynam. Earthq. Eng.* **28,** 387–404.

Todorovska, M. I., and M. D. Trifunac (2008b). Impulse response analysis of the Van Nuys 7-story hotel during 11 earthquakes and earthquake damage detection, *Struct. Control Health Monit.* **15,** 90–116.

Trifunac, M. D. (1972). Comparisons between ambient and forced vibration experiments, *Earthq. Eng. Struct. Dynam.* **1,** 133–150.

Trifunac, M. D., S. S. Ivanović, and M. I. Todorovska (2001a). Apparent periods of a building. I: Fourier analysis, *J. Struct. Eng.* **127,** no. 5, 517–526.

Trifunac, M. D., S. S. Ivanović, and M. I. Todorovska (2001b). Apparent periods of a building. II: Time-frequency analysis, *J. Struct. Eng.* **127,** no. 5, 527–537.

Tsai, V. C. (2011). Understanding the amplitudes of noise correlation measurements, *J. Geophys. Res.* **116,** no. B09311, doi: 10.1029/2011JB008483.

van der Neut, J., J. Thorbecke, K. Mehta, E. Slob, and K. Wapenaar (2011). Controlled-source interferometric redatuming by crosscorrelation and multidimensional deconvolution in elastic media, *Geophysics* **76,** no. 4, SA63–SA76, doi: 10.1190/1.3580633.

Vasconcelos, I., and R. Snieder (2008a). Interferometry by deconvolution, Part 1—Theory for acoustic waves and numerical examples, *Geophysics* **73,** no. 3, S115–S128.

Vasconcelos, I., and R. Snieder (2008b). Interferometry by deconvolution: Part 2—Theory for elastic waves and application to drill-bit seismic imaging, *Geophysics* **73,** no. 3, S129–S141.

Wapenaar, K. (2004). Retrieving the elastodynamic Green's function of an arbitrary inhomogeneous medium by cross correlation, *Phys. Rev. Lett.* **93,** 254–301.

Wegler, U., and C. Sens-Schönfelder (2007). Fault zone monitoring with passive image interferometry, *Geophys. J. Int.* **168,** 1029–1033.

Wegler, U., B.-G. Lühr, R. Snieder, and A. Ratdomopurbo (2006). Increase of shear wave velocity before the 1998 eruption of Merapi volcano (Indonesia), *Geophys. J. Int.* **33,** L09303, doi: 10.1029/2006GL025928.

Yamada, M., J. Mori, and S. Ohmi (2010). Temporal changes of subsurface velocities during strong shaking as seen from seismic interferometry, *J. Geophys. Res.* **115,** B03,302.

Appendix

Eigenfunctions and Eigenfrequencies of the String Model

In this appendix, we derive the eigenfunctions (expression 8) and eigenfrequencies (expression 9) of the string model (Fig. 6) using a perturbation analysis in the small parameter ϵ (expression 7). The normal modes of the unperturbed string ($\epsilon = 0$, $\rho_g = \infty$, and $R = -1$) are given by

$$u(z > 0) = \sin k^{(u)} z, \tag{A1}$$

$$u(z < 0) = 0, \tag{A2}$$

in which $k^{(u)}$ is the unperturbed wavenumber. The parameter ϵ accounts for the coupling of the light string to the heavy string (expression 6). For the unperturbed model ($\epsilon = 0$), the string has infinite mass for $z < 0$, and hence it does not move. When $\epsilon \neq 0$, the waveforms, which include perturbed waves, are expressed by

$$u(z > 0) = \sin kz + A \cos kz, \tag{A3}$$

$$u(z < 0) = Be^{-ik_g z}, \tag{A4}$$

respectively. The coefficients A and B depend on ϵ. According to expression (A4), waves are radiated downward in the lower (heavy) part of the string (the thick line in Fig. 6). The ratio of the wavenumbers in the light and heavy strings (k/k_g) is given by chapter 2 in Coulson and Jeffrey (1977):

$$k/k_g = \epsilon. \tag{A5}$$

The boundary conditions of the model are $\partial u/\partial z = 0$ at $z = H$, and u and $\partial u/\partial z$ are continuous at $z = 0$. From expressions (A3) and (A4) and these boundary conditions, we obtain

$$\frac{k}{k_g}\sin kH + i\cos kH = \frac{\epsilon}{2i}\left(e^{ikH} - e^{-ikH}\right) + \frac{i}{2}\left(e^{ikH} + e^{-ikH}\right) = 0, \tag{A6}$$

in which we use expression (A5) for k/k_g. From expression (A6), we obtain

$$e^{2ikH} = -\frac{1-\epsilon}{1+\epsilon}. \tag{A7}$$

Applying a first-order Taylor expansion in ϵ to the wavenumber in expression (A7), we obtain the wavenumber for mode m:

$$k_m = \left[\pm\left(m + \frac{1}{2}\right)\pi - i\epsilon\right]\frac{1}{H}, \tag{A8}$$

in which the real and imaginary of k_m are the unperturbed and perturbed parts of the wavenumber of mode m, respectively. The perturbation of the wavenumber caused by the radiation damping ($-i\epsilon/H$) is constant for all modes. The eigenfrequency ω_m that corresponds to the wavenumber in expression (A8) is given by expression (9).

From expressions (A3) and (A8), the waveform (eigenfunction) for the mode m within the light string is given by

$$\begin{aligned} u_m(z) &= \sin(k_m z) + A\cos(k_m z) \\ &= \sin(k_m z) + \frac{\cos(k_m H)}{\sin(k_m H)}\cos(k_m z) \\ &= \frac{\cos\{k_m(H-z)\}}{\sin(k_m H)}, \end{aligned} \tag{A9}$$

in which we use the boundary condition $\partial u/\partial z = 0$ at $z = H$ at the second equality. Using Taylor expansions to first order in ϵ in the sine and cosine functions, we derive the eigenfunction shown in expression (8).

Department of Geophysics
Stanford University
397 Panama Mall
Stanford, California 94305
nnakata@stanford.edu
(N.N.)

Center for Wave Phenomena
Department of Geophysics
Colorado School of Mines
1500 Illinois Street
Golden, Colorado 80401
rsnieder@mines.edu
(R.S.)

Manuscript received 23 February 2013;
Published Online 26 November 2013